Aeroacoustics Conferences
20-23 May 2019, Delft, The Netherlands
25th AIAA/CEAS Aeroacoustics Conference

10.2514/6.2019-2589



# Assessment of the Impact of a Heterogeneous Stator on the Noise of an Axial-Flow Low Mach-Number Stage

Miguel Pestana [1,2,3 (a)], Marlène Sanjosé [3 (b)],
Michel Roger [2 (c)], Stéphane Moreau [3 (d)], Mathieu Gruber [1 (e)]

[1] *Département Aérodynamique et Aéroacoustique*
*Safran Aircraft Engines, 77550 Moissy Cramayel, France*

[2] *Laboratoire de Mécanique des Fluides et d'Acoustique, UMR CNRS 5509*
*École Centrale de Lyon, Université de Lyon, 69134 Écully Cedex, France*

[3] *Université de Sherbrooke*
*Sherbrooke, J1K2R1, QC, Canada*



**The present work addresses the interaction noise of a small-size rotor-stator fan with heterogeneous Outlet-Guide-Vanes using the Lattice-Boltzmann Method. Three different meshes have been investigated to quantify the rotor-stator performance and noise sensibility with respect to the mesh refinement. With the increased mesh resolution, a vortex shedding on the rotor blades was put in evidence. The predicted aerodynamic performance is deteriorated with the intermediate mesh but greatly improved with the finest. The predicted noise levels were shown to be improved with the mesh refinement and are within two decibels at best with respect to the experiment. The finest mesh recovers a more accurate prediction of both broadband and tonal frequencies. In all cases, the same dominant modes were found to agree well with the measurements.**

## I. Introduction

Ultra High Bypass Ratio (UHBR) engines have the potential for significant reductions in fuel consumption, noise and emissions. However, this kind of architecture may require compact designs and a reduction of the nacelle size. In particular, shorter fan-OGV distances are expected in the near future. A solution is to hold the nacelle by structural elements included in the stator row, leading to geometrical and aerodynamic heterogeneities. Such new features would strongly modify the noise generation mechanisms. Firstly, the rotor-stator interaction will be stronger because of the shorter separation. Secondly, the heterogeneity may generate modes other than the so-called Tyler & Sofrin modes [1–4] characteristic of homogeneous architectures.

For both modeling and experimental convenience, assessing the effects of the heterogeneity on simple rotor-stator stages is relevant. The present work focuses on a low Mach-number ducted axial fan with several features of future modern fan-OGV architectures. Its tip Mach number at full power is around 0.3. Three stator vanes of the stage configuration are thicker than the others for structural reasons. This heterogeneity has been shown to be the cause of propagating modes that would not be excited in a homogeneous configuration [1, 5].

The influence of heterogeneous stators on the noise of the above low Mach-number ducted axial fan is investigated numerically with a LBM-VLES method. Preliminary results [1] showed that the stator heterogeneity is indeed responsible for the regeneration of the 1st and 2nd BPF that would be cut-off for homogeneous rotor and stator according to Tyler & Sofrin's rule. We now investigate in more detail the sensitivity of the operating point, predicted sound levels and modal content as functions of the mesh resolution. A previous study [1] evidenced a discrepancy in the

(a) PhD student, miguel.pestana@doctorant.ec-lyon.fr
(b) Research engineer
(c) Professor
(d) Professor
(e) Research engineer

predicted pressure rise of about 16% compared to the experiments. The objective is to investigate if a mesh refinement would influence the flow topology and consequently the operating point and to confirm that the heterogeneity is the only cause for the BPF regeneration.

The paper is organized as follows. First, the simulated facility and the numerical strategy are presented. Secondly, an aerodynamic analysis is given where the operating point and flow topology are detailed for each mesh grid. Finally, the acoustic analysis is detailed. In this investigation, spectra of wall-mounted microphones are compared to the experiments along with the calculated modal amplitudes.

## II. Simulated Setup and Numerical Strategy

### A. The Simulated Facility at Ecole Centrale de Lyon

The present fan is a HVAC fan used in the cargo hold and galley cooling of aircraft. It is installed in an experimental test facility at École Centrale de Lyon dedicated to accurate measurements. The duct is instrumented with both acoustic and aerodynamic sensors. A sketch of the test facility is shown in Figure 1.

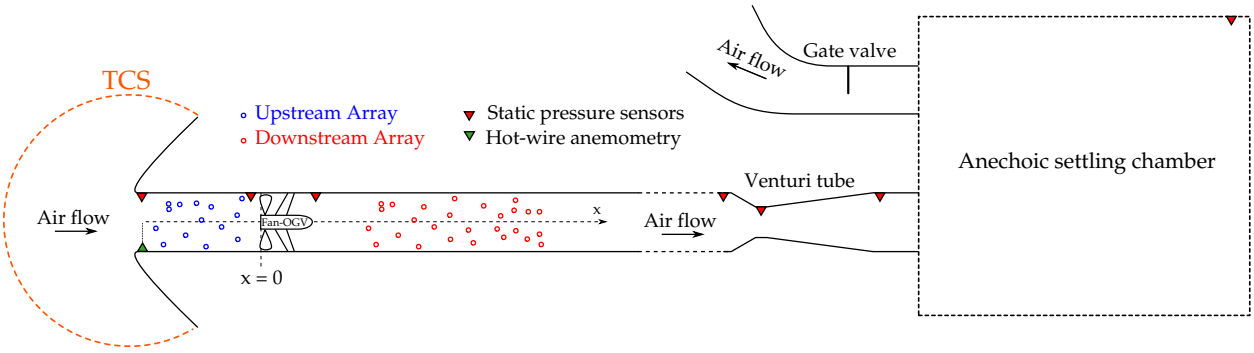


**Fig. 1 Sketch of the experimental setup at École Centrale de Lyon. Arrays of wall-mounted microphones shown as blue and red circles.**

The fan is made of $B = 17$ rotor blades and $V = 23$ stator vanes, three of which are thicker, see Figure 2. It is important to note that the degree of heterogeneity for this configuration can be considered to be weak. In fact, the heterogeneous stator vanes are only thicker by a factor of three at the tip but are identical at the hub. A power-supply cable is also placed downstream of one of the heterogeneous stator vanes, see Figure 2(b). This cable may cause an additional potential distortion. The distance between the rotor blade trailing edge and the stator vane leading edge varies from $0.79c_r$ at the hub to $1.14c_r$ at the tip where $c_r$ is the rotor blade chord. Because of the short rotor-stator distance, rotor blades are possibly perturbed by the potential field from the stator vanes. The hub to tip ratio is around 0.55.

The objective is to simulate this experiment numerically by using the Lattice-Boltzmann Method (LBM). For this reason, the same acoustic arrays as in the experiment are added in the simulation for a better comparison (wall-mounted probes upstream and downstream of the fan-OGV shown in Figure 1).

### B. The Numerical Strategy

The present LBM simulations use Powerflow 5.3b developed by Dassault Systems. The approach is naturally transient and compressible, providing a direct insight into hydrodynamic mechanisms responsible for the acoustic emission but also into acoustic propagation.

Instead of studying macroscopic fluid quantities, the LBM tracks the time and space evolution on a lattice grid of a truncated particle distribution function. The particle distribution evolution is driven to equilibrium by the so-called collision operator, approximated by the Bhatnagar-Gross-Krook model. The discretized Lattice-Boltzmann equations

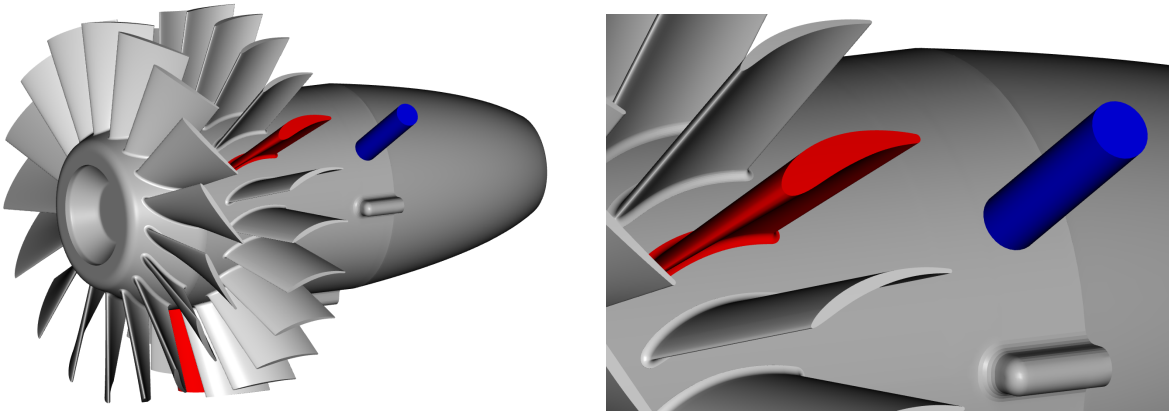

(a) Rotor-stator geometery.

(b) Zoom on one modified stator vane.

**Fig. 2 Fan geometry. Courtesy of Safran Ventilation Systems.**

need to be solved for a finite number of particle velocities. The discretization retained in Powerflow involves 19 discrete velocities for the third order truncation of the particle distribution function, which has been shown sufficient to recover the Navier-Stokes equations for a perfect gas at low Mach number in isothermal conditions [6–8]. In Powerflow, a single relaxation time is used, related to the dimensionless laminar kinematic viscosity [9]. For large Reynolds-number flows, a Very Large Eddy Simulation mode is used in which the relaxation time is replaced by an effective turbulent relaxation time that is derived from a systematic Renormalization Group procedure detailed in Chen *et al.* [10]. It captures the large structures in the room (included in the computational domain) but also the small turbulent scales (resolved on the simulation grid) that develop along the blade and duct surfaces. At the wall, the shear stress is modeled by the use of a wall-law boundary condition accounting for pressure gradients by means of specular reflections [11]. The particular extension of the method developed for rotating machines can be found in Zhang *et al.* [12].

*1. Numerical Setup and Mesh Levels*

In order to accurately investigate the noise-generating mechanisms, the whole test facility at École Centrale de Lyon presented in the previous section is numerically simulated with some minor simplifications, see Figure 3.

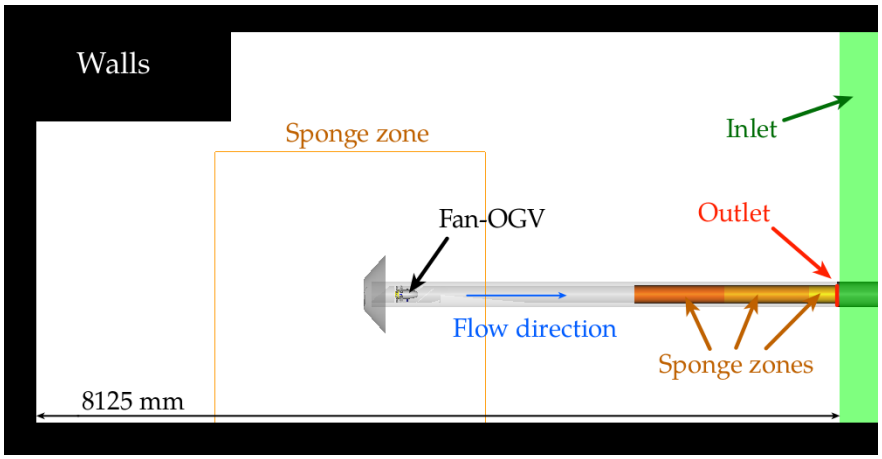


**Fig. 3 Simulation domain.**

The domain size is chosen according to the real room dimensions. However, the Venturi tube is replaced by a straight duct section and the ejection system removed (Figure 1). The experiments performed at École Centrale de

Lyon have evidenced a negligible level of the reflected waves at the duct termination. For this reason, sponge zones are introduced in the duct in order to mimic the effect of the settling chamber. In addition to that, a sponge zone is added in the fluid domain far from the inlet in order to avoid unrealistic hard-wall reflections in the room. Indeed, the walls are covered with absorbing materials in the experiment. The air is re-introduced in the room through the whole back-wall referred to as 'Inlet' in Figure 3 showing a side view of the simulated domain.

The imposed outlet boundary condition is a uniform velocity profile in the duct cross-section in order to obtain the desired mass-flow rate. This boundary condition has been shown to limit the numerical acoustic reflections. The inlet boundary condition sets a characteristic static pressure (measured atmospheric pressure in the experiments) along with free flow direction.

Three different mesh grids are investigated in this study and are defined in Table 1. The first mesh level (L0) has been investigated in a previous study [1] where both homogeneous and heterogeneous stator configurations where simulated. It has been shown that the heterogeneity was the cause for the emergence of the first two BPF that should be cut-off for a perfectly periodic stator. In this study, two additional mesh refinements are performed for the heterogeneous stator configuration. The refinement is done at the rotor and stator walls by adding volumes of finer resolution, see Figure 4. The mesh L0 has a minimum voxel size of 0.3 mm. The size is then reduced to 0.15 mm and 0.075 mm for the mesh levels L1 and L2 respectively. With these refinements, the maximum $y^+$ at the rotor blades is decreased from 70 to around 23. The remaining parts of the grid are kept identical in the three mesh configurations. The main simulation parameters are summarized in Table 1. Simulations are done at one nominal operating condition of the fan of mass flow rate $Q_0$ and pressure rise $\Delta P_0$.

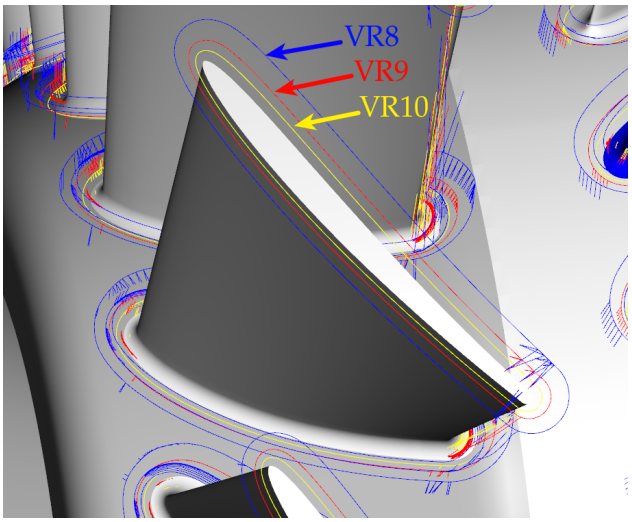


**Fig. 4 Different areas of mesh refinement close to the walls.**

## III. Aerodynamic Investigation

### A. Operating Conditions

First, the compressor map for three different operating conditions on the mesh level L0 is compared with the experiments in Figure 5. As previously mentioned, the pressure rise is underestimated. Nevertheless, the same slope (shown as continuous line between symbols) is retrieved. From observation of the blade and vane loads, important flow separations occurring on the stator [1] are the cause for the pressure rise mismatch. The mesh level L1 provides lower pressure rise. However, in this case, vortex shedding appearing on the rotor seems to coincide with a loss of performance of the rotor. This point is discussed in section III.B. Regarding the mesh level L2, the pressure rise is better recovered with a reduction of the error from 16% to 8%. In this mesh, the vortex shedding is attenuated.

| Mesh level | | **L0** | **L1** | **L2** |
|---|---|---|---|---|
| Number of refinement volumes | VR | 8 | 9 | 10 |
| Minimum voxel size [mm] | $\Delta x$ | 0.3 | 0.15 | 0.075 |
| Dimensionless wall distance | $y^+_{\max}$ (rotor) | 70 | 39 | 23 |
| | $y^+_{\max}$ (stator) | 45 | 28 | 15 |
| Timestep [s] | $\Delta t$ | $4.943 \times 10^{-7}$ | $2.471 \times 10^{-7}$ | $1.236 \times 10^{-7}$ |
| Mesh size | $N_{\text{voxels}}$ | $\sim 50 \times 10^6$ | $\sim 89 \times 10^6$ | $\sim 233 \times 10^6$ |
| Converged simulated time | $T_s \times \Omega/60$ | 21 | 12 | 2 |
| Reynolds number | $\text{Re}_D$ | 327795 | | |
| Tip Mach number | $M_{\text{tip}}$ | 0.26 | | |

**Table 1 Simulation parameters.**

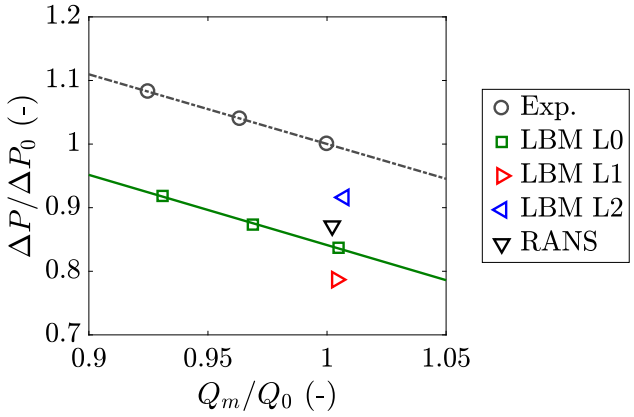


**Fig. 5 Compressor map for the different mesh levels compared to the experiments and RANS simulations.**

For a better insight into the rotor and stator performances, the axial pressure evolution is shown in Figure 6. The pressure rise is calculated from the point just upstream of the fan and from the last point as in experiments.

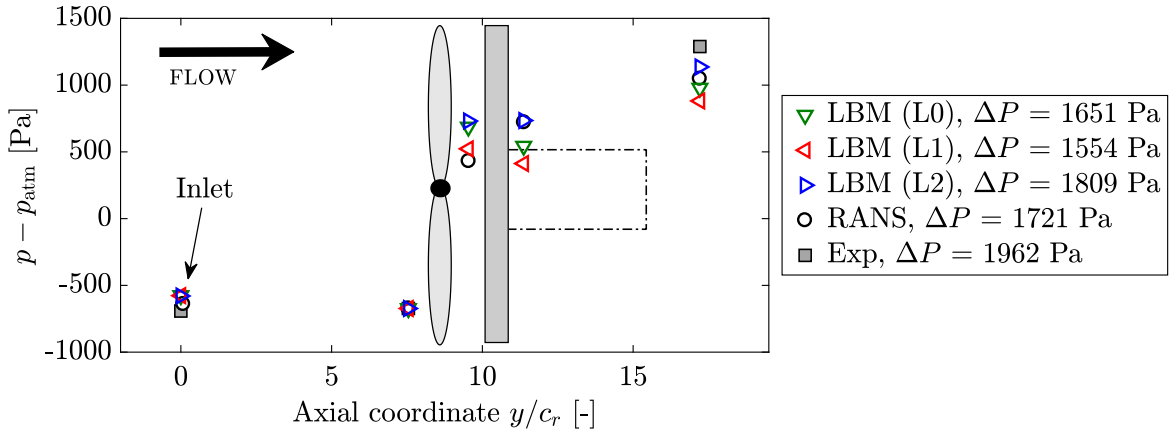


**Fig. 6 Numerical extractions for acoustic and aerodynamic analyses.**

For the mesh L0, the pressure rise is only achieved by the rotor. The flow across the stator row is observed to decrease the static pressure levels. As mentioned before, important pressure losses from massive flow separations seem to overwhelm the pressure recovery from the flow straightening in the stator, thus generating an overall static pressure

loss. For the mesh L1, the performance deteriorates through the rotor due to this enhanced instability. Through the stator, the same behavior as for the mesh L0 is observed leading to lower pressure. Finally, in the mesh L2, with the attenuation of the instability, the rotor performance is brought back to the levels obtained on mesh L0. In addition, the stator flow separations are greatly reduced with the mesh refinement. For this reason, no pressure loss is observed through the stator stage even though no significant increase is actually achieved.

Results are also compared with previous resolved RANS simulations of the same configuration [1, 5]. The RANS simulation was provided by University of Sherbrooke and has been performed with ANSYS CFX V15.0 using the standard $k-\omega$ SST [13] turbulence model and a second order spatial scheme. The domain's angular sector is reduced and accounts only for 3 rotor blades and 4 baseline stator vanes. The mesh consists of 27 millions cells and the boundary layer is fully resolved as the grid resolution is $y^+ = 2$ at the wall.

The obtained pressure rise is below the L2 mesh but higher compared with the L0 and L1 mesh. However, if we focus on the static pressure level just downstream of the OGV, the same pressure is obtained for the RANS and LBM (L2). The inaccuracy seems to come from the passage from the annular to the cylindrical duct where the LBM is seen to provide a higher pressure rise. One possibility would be to refine the mesh in the downstream region for the RANS case and investigate if any pressure increase is obtained. Nevertheless, the LBM and RANS simulations agree for the $\Delta P$ calculated from the pressure just upstream and downstream of the fan and OGV respectively.

### B. Vortex Shedding

As mentioned previously, a vortex shedding phenomenon is observed with the refined mesh and is discussed in this section. An instantaneous field of axial velocity for the mesh level L1 is shown in Figure 7. It can be clearly seen that some of the rotor blades are experiencing strong vortex shedding (highlighted in red). In fact, the better wall resolution compared with L0 yields the development of a boundary layer instability leading to the vortex shedding. A quick estimate of the vortex shedding frequency can be done with the simplified case of the cylinder. The Strouhal number (St) of 0.2 provides a frequency of:

$$f_s = \frac{\mathrm{St}\, U}{D} = 5778\,\mathrm{Hz} \tag{1}$$

where St = 0.2 and $U = 65$ m/s is the relative velocity at midspan. $D = 2.25$ mm is a rough estimate of the distance accounting for the trailing edge and boundary layer thicknesses (upper and lower).

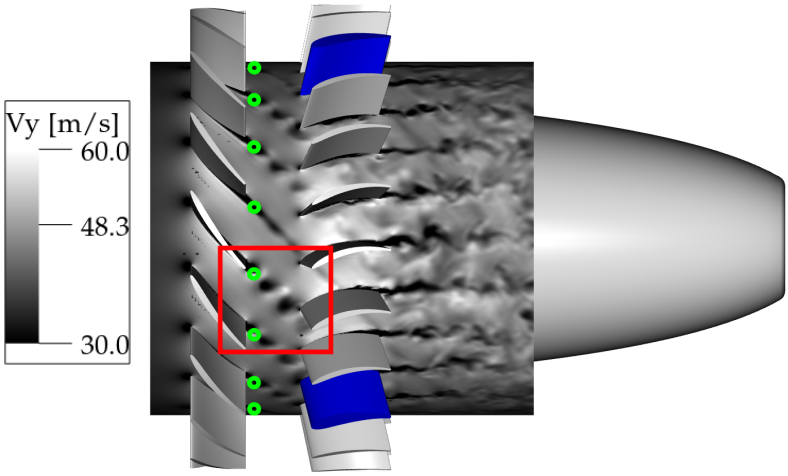


**Fig. 7 Cylindrical cut at midspan for the mesh L1. Vortex shedding is observed on some blades (highlighted in red). Probes in the rotating reference frame shown in green.**

For a clearer observation, signals from probes in the rotating reference frame and placed in the rotor wakes are shown in Figure 8. A periodic phenomenon is clearly seen in some blade wakes. The appearance of strong vortex

shedding only on some blades may be caused by mesh heterogeneities due to the Cartesian approach used by the LBM solver.

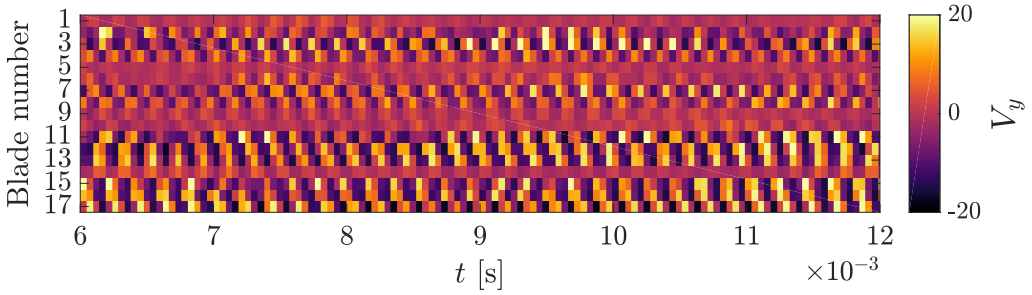


**Fig. 8 Axial velocity time signals of the wakes in the rotating reference frame at midspan for the L1 mesh.**

Figure 9 shows the spectrum of the axial velocity at one of the probes experiencing strong vortex shedding. A clear tone appears at a frequency roughly equal to 5200 Hz providing a shedding frequency not far from the previous analytical estimate.

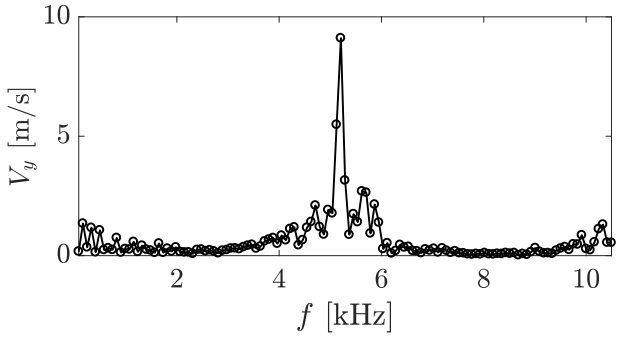


**Fig. 9 Spectrum of one axial velocity time signal where the vortex shedding is observed in the L1 mesh at midspan.**

Finally, vorticity fields at midspan are shown for the three meshes in Figure 10. In the finer mesh L2, the vortex shedding appearing on some blades is strongly attenuated. In addition, the flow downstream of the stator vanes is less oscillating and by analysis of the vane loading, some of the occurring flow separations are observed to be greatly attenuated. This is in accordance with what is observed on the pressure evolution shown in the previous section where the pressure loss through the stator stage is not observed anymore in the mesh L2. The better resolution of the small-scale turbulent features at the vane walls is observed to increase the efficiency of the overall OGV stage.

To conclude, the presence of vortex shedding agrees well with the predictions found in the literature for bluff bodies [14–16] at the considered Reynolds number range. In the presented case, the Reynolds number based on the distance $D$ for the rotor is approximately $10^4$. For such a turbulent subcritical case, the Strouhal number of 0.2 is usually found in the cited references. For these reasons, the observed vortex shedding in this configuration and at this operating point could be. Yet, the better wall resolution provided by the mesh L2 yields another boundary layer state that do not originate clear vortex shedding. In fact, the additional resolved small-scale turbulent structures in the mesh L2 do have a relevant impact on the boundary layer development. To sum-up, even if the vortex-shedding observed in the mesh L1 could be physical, it is probably generated from a peculiar boundary layer state given by the mesh L1 and is diminished with the additional smaller scales in the mesh L2.

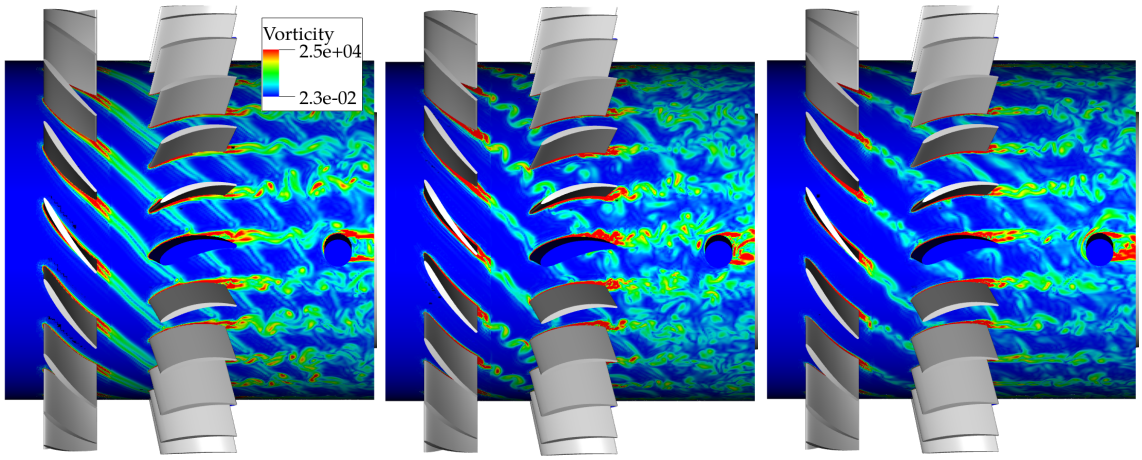


(a) Mesh L0. (b) Mesh L1. (c) Mesh L2.

**Fig. 10 Instantaneous vorticity fields for the meshes L0, L1 and L2 at midspan.**

## IV. Acoustic Investigation

In this section, the acoustic analysis is provided. The various spectra given by the different simulations and the experiment are shown in Figures 11 and 12. For fair comparisons between the different mesh resolutions and the experiment, the time signal length is cropped to the shortest one simulated on the mesh L2. The frequency resolution is around 80 Hz. First of all, the homogeneous stator configuration previously simulated [1] on the mesh level L0 shows an important cancellation of the first two BPFs by more than 8 dB. Better cancellation is obtained for the downstream array. This demonstrates that the heterogeneity of the stator is responsible for the 1st and 2nd BPF regeneration.

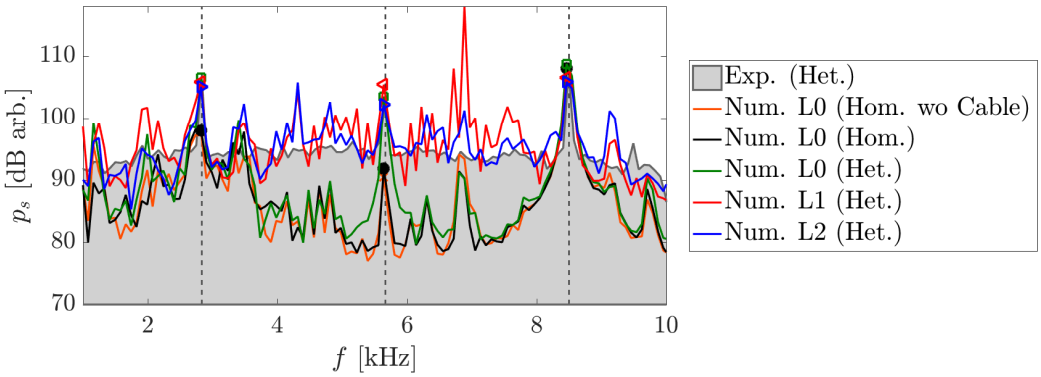


**Fig. 11 Averaged wall-spectra from probes of the upstream array for the experiments and the three simulated mesh levels. Arbitrary dB scale.**

The first mesh refinement (L1) is seen to increase the broadband levels, now matching the measurements. However, some important peaks appear at around 7 kHz. These tones are not well understood yet but could be related to the vortex shedding previously discussed. Due to the rotational speed, a modulation of the vortex shedding frequency will appear providing a different radiation frequency in the stationary frame of reference. In the mesh level L2, these peaks at 7 kHz are considerably reduced for the upstream array. The broadband level is nevertheless kept at a similar level compared to the mesh L1. For the downstream array, the unexpected peaks at 3.5 and 6 kHz remain for the finer mesh L2. Further investigation is needed before concluding on the precise origin of these peaks.

In order to estimate more precisely the BPF levels, a re-sampling of the time signals is done to perform averages

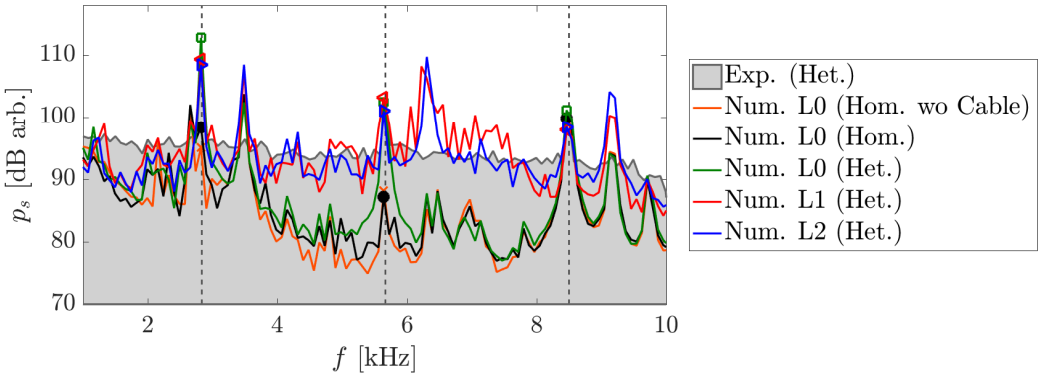


**Fig. 12 Averaged wall-spectra from probes of the downstream array for the experiments and the three simulated mesh levels. Arbitrary dB scale.**



on synchronized revolutions. The result provides a spectrum with only harmonics of the rotational speed and where BPF levels have been recovered. Results are shown in Figure 13.

The mesh refinement provides a more accurate BPF prediction in all cases. Regarding the BPF 1 level, the higher mesh resolution reduces the overestimation to about 2 dB in the upstream array. For the second and third BPF, the recovered level is within 1 dB. In the downstream array, the same overestimation of the BPF 1 is seen to be reduced when refining. For the mesh L2, results are within 3 dB compared with experiments.

Interestingly, similar BPF dynamics as in experiments are captured. On the one hand, the first two BPFs have lower levels compared with the third one for the upstream array. On the other hand, levels are monotonically decreasing for the downstream array. The important differences in level between the upstream and downstream arrays may be explained by combinations of the modal angle and the equivalent dipole radiation angle of the stator vane. An amplification is observed when the modal angle is not far from the dipole angle and a reduction is observed otherwise.

Finally, the homogeneous case hidden by the chosen range level for the first two BPFs is seen to be below the heterogeneous level by more than 15 dB. The synchronized average performed on the signals put in evidence a greater cancellation of the BPF levels.

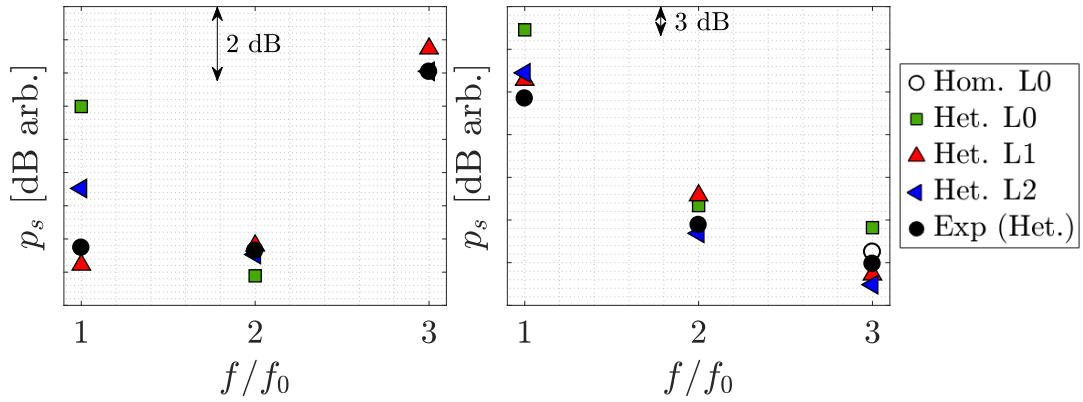


(a) Upstream (b) Downstream

**Fig. 13 BPF levels calculated using re-sampled time signals. The level range was adjusted to the heterogeneous configurations. Levels at the first two BPFs are more than 15 dB below. Arbitrary dB scale.**

### A. Modal Decomposition at the Blade Passing Frequencies

Finally, modal decompositions are performed using the measured pressure fluctuations acquired by each array shown in Figure 1. The objective of this modal decomposition is to assess the modal content of the fan module and to investigate which modes are predominant [17–24]. It is expected that modes related to the stator heterogeneity at the first two BPFs (cut-off in a homogeneous configuration) will be highlighted for all mesh levels. Considering a rigid-wall duct of circular cross-section, the acoustic pressure at any point inside the duct can be expressed as a sum of annular modes as follows [25, 26]

$$p(x,r,\theta,t) = \sum_{m=-\infty}^{+\infty} \sum_{n=0}^{+\infty} \frac{f_{mn}(r)}{\Gamma_{mn}} \left[ A_{mn}^{+} \mathrm{e}^{\mathrm{i}\gamma_{mn}^{+} x} + A_{mn}^{-} \mathrm{e}^{\mathrm{i}\gamma_{mn}^{-} x} \right] \mathrm{e}^{\mathrm{i}m\theta} \mathrm{e}^{-\mathrm{i}\omega t}, \tag{2}$$

where the pressure $p$ is measured (known), $A_{mn}^{\pm}$ are the modal amplitudes (unknowns) [27] and $f_{mn}$ the radial shape functions. A detailed description of the modal basis parameters is given in Appendix A. The time signals used to perform the modal decompositions are also averaged over the revolutions (engine order analysis). Because the focus is put on BPFs, this method allows achieving higher number of averages with short signals as for the finest mesh L2.

Results are shown in Figure 14 for the upstream array and in Figure 15 for the downstream array. First of all, the only radiating mode for the homogeneous configuration is the mode $m = 5$ observed at the third BPF. It is a Tyler & Sofrin's mode given by the simple rule $m = sB - pV$.

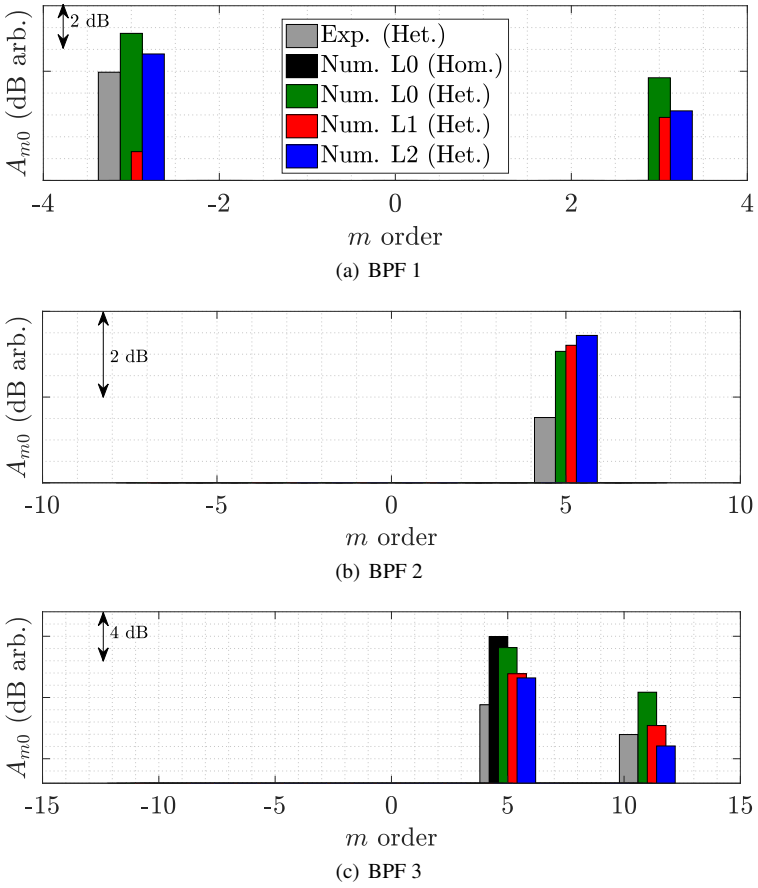


(a) BPF 1

(b) BPF 2

(c) BPF 3

**Fig. 14 Azimuthal modal content at the first three blade passing frequencies and radial order $n = 0$ upstream of the fan. Arbitrary dB scale.**

For the heterogeneous stator, acoustic modes can be identified at the first two BPFs. At the first BPF, the modes $m = -3$ and $m = 3$ are observed in the simulations while in the experiments only the mode $m = -3$ is observed. In

previous experiments on the same configuration, a slight difference in the operating conditions has evidenced switch of dominant mode between the modes -3 and 3. Because in the simulations the operating point was seen to slightly vary, the same phenomenon could be at the origin of this inversion. Moreover, because the mode is close to its cut-off limit, it is very sensitive to small variations of the flow. Nevertheless, the predicted levels are in good agreement with the experiments. At the second BPF, the mode $m = 5$ is dominant. For the downstream array, the mesh refinement is seen to play an important role and considerably reduces the error. Finally, at the third BPF, the mode amplitude is decreased with the mesh refinement, thus decreasing the gap with the experiments. The mode $m = 11$ attributed to the stator heterogeneity is well captured for the upstream array but is not seen as dominant for the downstream array. This is in good agreement with the experiments where the same behavior is observed. To conclude, the overall prediction of the dominant modes is not sensitive to the mesh level. However, the refinement of the mesh grid improves the prediction accuracy of some modes.

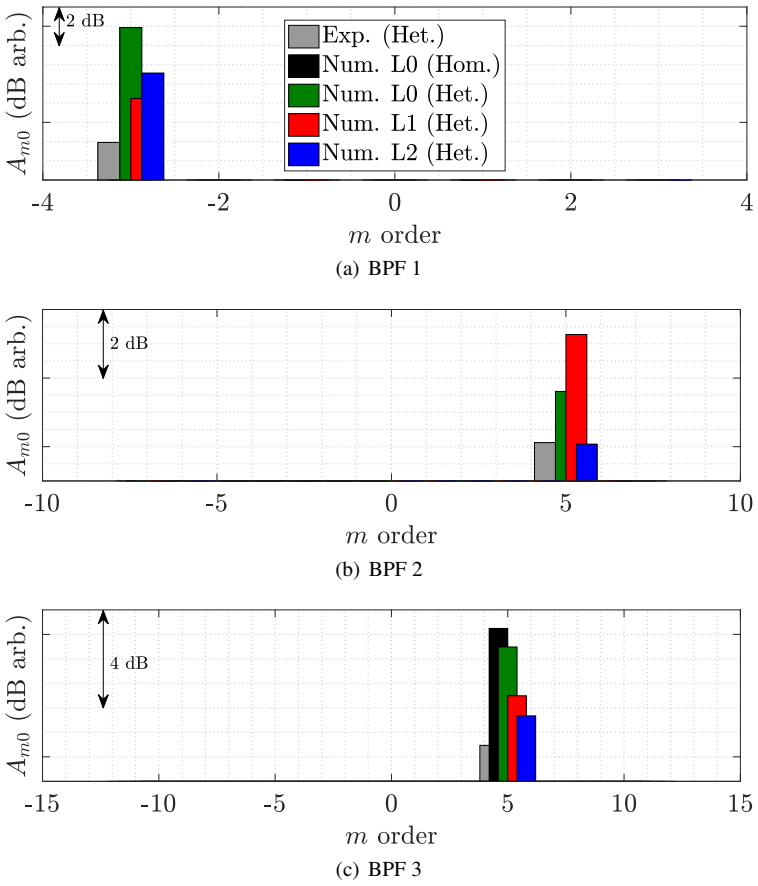


(a) BPF 1

(b) BPF 2

(c) BPF 3

**Fig. 15 Azimuthal modal content at the first three blade passing frequencies and radial order $n = 0$ downstream of the fan. Arbitrary dB scale.**

Regarding the radial modes energy distribution not shown here, the majority of the energy is found to be at the order $n = 0$. This is partly due to the fact that higher radial orders are often cut-off for the identified dominant modes and at these operating conditions.

## V. Concluding Remarks

In this study, different mesh resolutions have been simulated with the LBM approach allowing to investigate the sensibility of the operating point and predicted sound spectra of a rotor-stator fan stage with respect to the mesh refinement. A considerable improvement has been obtained for the finer mesh with the pressure rise error being

reduced compared with the experiments. With the mesh refinement, a vortex shedding is evidenced. Even if this phenomenon agrees with what is predicted in the literature for the considered local Reynolds numbers, it is thought here to be generated by a particular boundary layer state found in the mesh L1. In fact, the increased near-wall resolution of the finest mesh leads to an important attenuation of this phenomenon. In terms of acoustics, the refinement of the mesh allows better recovering the experimental broadband levels. Regarding the modal content, the same dominant modes are well captured by all meshes. Nevertheless, the discrepancies with the measurements are in general reduced for the finer mesh. In fact, the overestimation of the third BPF for the coarser mesh is greatly reduced. These results stress that the observed dominant modes are due to the stator heterogeneity and do not depend on the mesh resolution. The main expected noise mechanism which is the wake interaction is finally not seen to be very sensitive to the flow topology variations. In fact, the results on the different meshes at worst show level variations within 4 dB.

## Acknowledgments

The authors thank Université de Lyon for providing the necessary computational resources and for the technical support. The authors also acknowledge Damiano Casalino and Ignacio Gonzalez-Martino from Exa for the help in setting-up the simulation. This work was performed within the framework of the industrial Chair ADOPSYS co-financed by Safran Aircraft Engines and the ANR (ANR-13-CHIN-0001-01) and is also supported by the Labex CeLyA of the Université de Lyon, within the programme 'Investissements d'Avenir' (ANR-10-LABX-0060/ANR-16-IDEX-0005) operated by the French National Research Agency (ANR).



## A. Appendix: Duct Modal Basis Parameters

Parameters of the duct modal basis are given in this appendix. Radial shape functions for a cylindrical duct are defined as

$$f_{mn}(r) = J_m(K_{mn}r) \tag{3}$$

where $K_{mn}$ are the hard-walled duct eigenvalues. The radial shape normalization factors are given by

$$\Gamma_{mn} = \int_{R_{\text{hub}}}^{R_{\text{tip}}} f_{mn}(r)^2 r \mathrm{d}r = \pi \left[ r^2 f_{mn}^2(r) \left( 1 - \frac{m^2}{K_{mn}^2 r^2} \right) \right]_{R_{\text{hub}}}^{R_{\text{tip}}} \tag{4}$$

The wave numbers $\gamma_{mn}^{\pm}$ are defined as

$$\gamma_{mn}^{\pm} = \frac{M_0 k_0}{\beta^2} \pm \frac{k_{mn}}{\beta^2} \tag{5}$$

with $\beta = \sqrt{1 - M_0^2}$, $k_0 = \omega / U_0$ and the axial wave number given by

$$k_{mn} = \sqrt{k_0^2 - \beta^2 K_{mn}^2} \tag{6}$$

## References

[1] Pestana, M., Sanjosé, M., Moreau, S., Roger, M., and Gruber, M., "Investigation on the noise of an axial low Mach-number fan stage with a heterogeneous stator," Fan Noise 2018, 2018.

[2] Sanjose, M., Pestana, M., Moreau, S., and Roger, M., "Influence and modeling of OGV heterogeneity," 22nd AIAA/CEAS Aeroacoustics Conference, 2016, p. 2881.

[3] Bonneau, V., Polacsek, C., Barrier, R., Lewy, S., Roux, J.-M., and Gervais, Y., "Tonal Noise Prediction of a Turbofan with Heterogeneous Stator and Bifurcations," AIAA Journal, Vol. 53, No. 11, 2015, pp. 3354–3369.

[4] Roger, M., and Caule, P., "Assessement of the Effect of Stator Inhomogeneity on Rotor-Stator Tonal Noise," ISROMAC-15, 2014.

[5] Pestana, M., Pereira, A., Salze, E., Thisse, J., Sanjosé, M., Jondeau, E., Souchotte, P., Roger, M., Moreau, S., Regnard, J., and Gruber, M., "Aeroacoustics of an axial ducted low Mach-number stage: numerical and experimental investigation," 23rd AIAA/CEAS Aeroacoustics Conference, 2017, p. 3215.

[6] Frisch, U., D'Humiéres, D., Hasslacher, B., Lallemend, P., Pomeau, Y., and Rivet, J.-P., "Lattice gas hydrodynamics in two and three dimensions," Complex Syst., Vol. 1, 1987, pp. 649–707.

[7] Chen, S., and Dooler, G. D., "Lattice Boltzmann method for fluid flows," Ann. Rev. Fluid Mech., Vol. 30, 1998, pp. 329–364.

[8] Marié, S., Ricot, D., and Sagaut, P., "Comparison between lattice Boltzmann method and Navier-Stokes high order schemes for computational aeroacoustics," J. Comp. Phys., Vol. 228, 2009, pp. 1056–1070.

[9] Vergnault, E., Malaspinas, O., and Sagaut, P., "A lattice Boltzmann method for nonlinear disturbances around an arbitrary base flow," J. Comput. Phys., Vol. 231, 2012, pp. 8070–8082.

[10] Chen, H., Orszag, S. A., Staroselsky, I., and Succi, S., "Expanded analogy between Boltzmann kinetic theory of fluids and turbulence," J. Fluid Mech., Vol. 519, 2004, pp. 301–314.

[11] Chen, H., Teixeira, C., and Molvig, K., "Realization of Fluid Boundary Conditions via Discrete Boltzmann Dynamics," International Journal of Modern Physics C, Vol. 09, No. 08, 1998, pp. 1281–1292. doi:10.1142/S0129183198001151, URL http://www.worldscientific.com/doi/abs/10.1142/S0129183198001151.

[12] Zhang, R., Sun, C., Li, Y., Satti, R., Shock, R., Hoch, J., and Chen, H., "Lattice Boltzmann Approach for Local Reference Frames," Commun. Comput. Phys., Vol. 9, No. 5, 2011, pp. 1193–1205.

[13] Menter, F., Kuntz, M., and Langtry, R., "Ten years of industrial experience with the SST turbulence model," Turbulence, heat and mass transfer, Vol. 4, No. 1, 2003, pp. 625–632.

[14] Etkin, B., and Ribner, H. S., "Canadian research in aerodynamic noise," Tech. rep., University of Toronto, 1958.

[15] Bearman, P., "On vortex shedding from a circular cylinder in the critical Reynolds number regime," Journal of Fluid Mechanics, Vol. 37, No. 3, 1969, pp. 577–585.

[16] Achenbach, E., and Heinecke, E., "On vortex shedding from smooth and rough cylinders in the range of Reynolds numbers 6× 10 3 to 5× 10 6," Journal of fluid mechanics, Vol. 109, 1981, pp. 239–251.

[17] Farassat, F., Nark, D. M., and Thomas, R. H., "The Detection of Radiated Modes From Ducted Fan Engines," 7th AIAA/CEAS Aeroacoustics Conference, Maastricht, The Netherlands, 2001, 2001.

[18] Rademaker, E., Sijtsma, P., and Tester, B., "Mode detection with an optimised array in a model turbofan engine intake at varying shaft speeds," 7th AIAA/CEAS Aeroacoustics Conference and Exhibit, 2001, p. 2181.

[19] Enghardt, L., Neuhaus, L., and Lowis, C., "Broadband sound power determination in flow ducts," 10th AIAA/CEAS Aeroacoustics Conference, American Institute of Aeronautics and Astronautics, 2004. URL http://eprints.soton.ac.uk/10419/, aIAA 2004-2940.

[20] Lewy, S., "Inverse method predicting spinning modes radiated by a ducted fan from free-field measurements," The Journal of the Acoustical Society of America, Vol. 117, No. 2, 2005, pp. 744–750. doi:http://dx.doi.org/10.1121/1.1850208, URL http://scitation.aip.org/content/asa/journal/jasa/117/2/10.1121/1.1850208.

[21] Castres, F. O., and Joseph, P. F., "Experimental investigation of an inversion technique for the determination of broadband duct mode amplitudes by the use of near-field sensor arrays," The Journal of the Acoustical Society of America, Vol. 122, No. 2, 2007, pp. 848–859. doi:http://dx.doi.org/10.1121/1.2747166, URL http://scitation.aip.org/content/asa/journal/jasa/122/2/10.1121/1.2747166.

[22] Castres, F. O., and Joseph, P. F., "Mode detection in turbofan inlets from near field sensor arrays," The Journal of the Acoustical Society of America, Vol. 121, No. 2, 2007, pp. 796–807. doi:http://dx.doi.org/10.1121/1.2427124, URL http://scitation.aip.org/content/asa/journal/jasa/121/2/10.1121/1.2427124.

[23] Bennett, G. J., O'Reilly, C., Tapken, U., and Fitzpatrick, J., "Noise source location in turbomachinery using coherence based modal decomposition," Proceedings of the 15th AIAA/CEAS Aeroacoustics Conference, Miami, FL, USA, 2009.

[24] Tapken, U., Raitor, T., and Enghardt, L., "Tonal Noise Radiation From an UHBR Fan - Optimized In-Duct Radial Mode Analysis," Proceedings of the 15th AIAA/CEAS Aeroacoustics Conference, Miami, FL, USA, 2009.

[25] Munjal, M., Acoustics of Ducts and Mufflers With Application to Exhaust and Ventilation System Design, Wiley-Interscience publication, Wiley, 1987. URL https://books.google.fr/books?id=Z-s50vk-U68C.

[26] Rienstra, S., and Hirschberg, A., "An introduction to acoustics," Report IWDE, 2001.

[27] Pereira, A., Finez, A., Leclere, Q., Salze, E., and Souchotte, P., "Modal identification of a small-scale ducted fan," 22nd AIAA/CEAS Aeroacoustics Conference, 2016, p. 3063.